

Journal Homepage: - www.journalijar.com

INTERNATIONAL JOURNAL OF ADVANCED RESEARCH (IJAR)

AVTERNATIONAL AVERNAL OF ADTANCED RESEARCH GLARI

STORY OF THE ST

Article DOI:10.21474/IJAR01/22077 **DOI URL:** http://dx.doi.org/10.21474/IJAR01/22077

RESEARCH ARTICLE

FREQUENCY RESPONSE OF THIN TOROIDAL INDUCTORS: A HYBRID APPROACH COMBINING THEORY, SIMULATION AND MEASUREMENT

R. Solalta¹, M. Koularambaye² and D.D. Yaya³

.....

- 1. High School of Excellence No. 1, Sarh, Chad.
- 2. Polytechnic University of Mongo, Chad.
- 3. National Higher Institute of Science and Technology of Abeche, Chad.

Manuscript Info

Manuscript History

Received: 21 August 2025 Final Accepted: 23 September 2025

Published: October 2025

Key words:-

Thin toroidal inductor, frequency response, hybrid modeling, experimental characterization, High-frequency optimisation.

Abstract

This paper investigates the frequency response of a thin toroidal inductor (200 $\mu m)$ made of 4C65 ferrite and wound with 18 turns. A hybrid methodology combining analytical modeling, numerical simulati on using HFSS, and experimental characterization with a 6500B impedance analyzer. The analysis focuses on two key parameters: the self-inductance (L) and the series resistance (R) as functions of frequency. The comparative study between theoretical, simulated, and measured results demonstrates that the inductance remains close to 1 μH over the 1 MHz–10 MHz range. The DC resistance (R_{DC}) is approximately 12 m Ω , while the simulated and measured AC resistances (R_{AC}) exhibit good agreement. However, analytical models show noticeable deviations beyond approximately 1 MHz, revealing their limitations in predicting high-frequency behavior.

"© 2025 by the Author(s). Published by IJAR under CC BY 4.0. Unrestricted use allowed with credit to the author."

Introduction:-

Modern power electronics favors compact, high-performance components for high-frequency operation. Thin toroidal inductors offer strong integration potential, but their modeling is challenging due to skin effect, proximity effect, and parasitic capacitances. Existing analytical models, although numerous, show limitations for very thin cores, where electromagnetic and capacitive couplings dominate. This work proposes a hybrid approach combining theoretical modeling, 3D simulation, and experimental characterization. The study focuses on a toroidal NiZn ferrite inductor (4C65, 200 µm, 18 turns) to characterize its frequency behavior and assess the validity of existing models, aiming to provide a reliable framework for high-frequency inductor optimization.

Methodology and Materials:-

The methodology proposed in this study consists of characterizing a toroidal inductor with a magnetic core by measuring its inductance and series resistance using a 6500B impedance analyzer. A hybrid approach combining analytical calculations, numerical simulations, and experimental measurements is implemented to provide a comprehensive understanding of the component's frequency-dependent behavior.

Target Structure and Component Parameters:

The target structure (Figure 1) is a toroidal inductor (NiZn ferrite, 4C65) with a closed rectangular-shaped cross-section and a reduced thickness of approximately $200 \mu m$. The conductor used is an enameled copper wire with a circular cross-section.

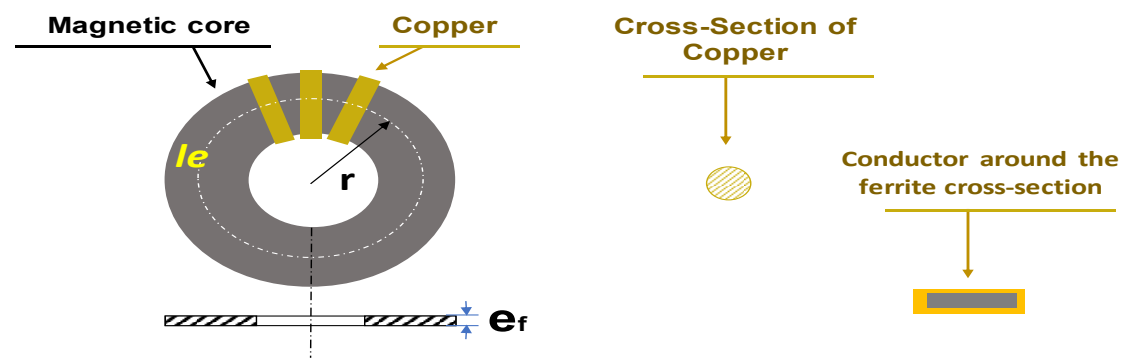


Figure 1: Target Structure and Parameters.

The component's characteristics are summarized in the following table:

Table 1: Component Characteristics

Parameter	Symbol	Value	Unit
Outer/Inner Diameter	d_o/d_i	36.25/22.75	mm
Ferrite Cross-Section	A	6.75 x 0.20	mm²
Mean Length	l _e	89.7	mm
Initial Perméability	$\mu_{\rm i}$	125	-
Copper Winding Cross-Section	S_{Cu}	0.44	mm ²
Number of Turns	N	18	
Copper Length	1	311	mm

Analytical Models:

Self-Inductance Coefficient L:

For a toroidal structure with a closed magnetic circuit, the analytical model of the inductance L depends on the relative permeability μr of the magnetic material, the number of turns N, and the geometric parameters of the magnetic core.

Conventionally, this value is calculated using the following formula:

$$L = \mu_r \mu_0 N^2 \frac{A_e}{I_e} = \mu_r \mu_0 N^2 \frac{A_e}{\pi (r_i + r_0)} \quad [H]$$
 (1)

where μ_r and μ_0 are the relative permeability of the material and of vacuum, respectively ($\mu_0 = 4\pi \times 10^{-7}$ H/m). As is the effective core cross-sectional area. r_i and r_0 are the inner and outer radius of the toroidal core.

For thin components such as integrated inductors, the magnetic circuit has a square cross-section, as in our case, with relatively small thicknesses (ranging from a few tens to several hundred micrometers). To predict the inductance of such components, some authors [1] use the following logarithmic formula:

$$L_{core} = \mu_r \mu_0 N^2 \frac{t_{core}}{2\pi} ln \left(\frac{d_o}{d_i}\right)$$
 [H]

Where t_{core} represents the thickness of the magnetic circuit.

The adaptation of these two models to our component, considering a frequency-dependent permeability, yields the following results:

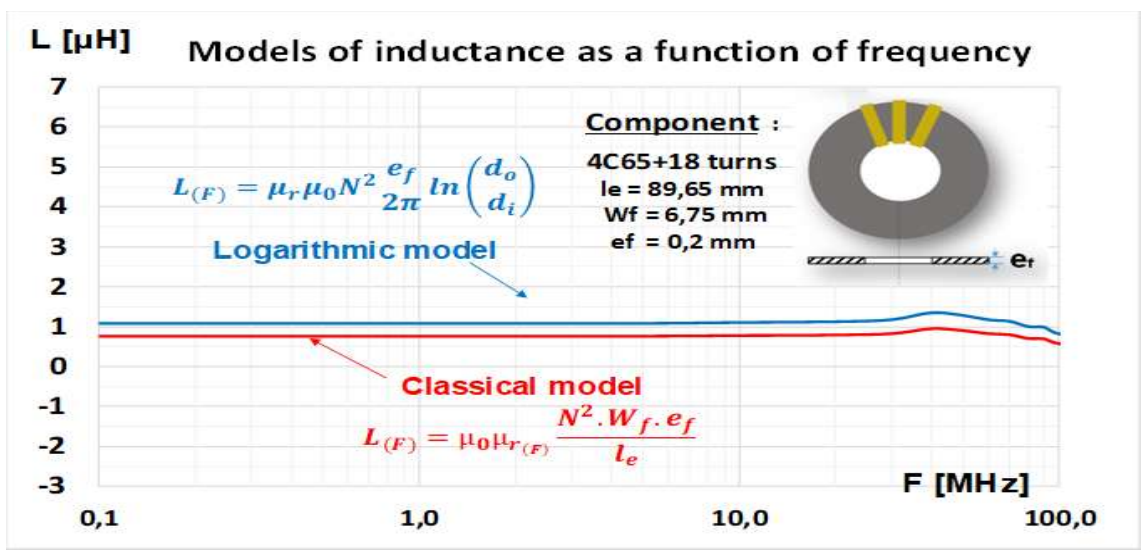


Figure 2: Inductance Models as a Function of Frequency.

Figure 2 shows that the inductance remains nearly constant from 100 kHz up to several tens of MHz, corresponding to the linear operating region of the magnetic circuit. It should be noted that the logarithmic model predicts inductance values approximately 0.3 µH higher than those obtained with the classical model.

Series Resistance R:

The series resistance accounts for the DC resistance (RDC) of the conductor, the influence of the magnetic material's resistivity, and the skin and proximity effects, which become significant at high frequencies.

The DC resistance, or low-frequency resistance, is the main source of copper losses, as it dissipates energy in the form of heat. It can be calculated from the resistivity ρ of the conductor, its cross-sectional area S_{Cu} , and its total length l, as follows:

$$R_{DC} = \rho_{Cu} \frac{1}{S_{Cu}} \quad [\Omega]$$
 (3)

With the resistivity of copper being $\rho \approx 1.68 \times 10^{-8} \ \Omega \cdot m$, applying this formula yields $R_{DC} \simeq 12 \ m\Omega$.

Skin Effect:

When the conductor carries a time-varying current (Figure 3), it generates a varying magnetic field around it. Variations in this field induce eddy currents toward the periphery of the conductor. Part of this current flows preferentially (in the same direction as the main current) within a depth δ , known as the skin depth. As a result, the effective cross-section of the conductor decreases, increasing its resistance.

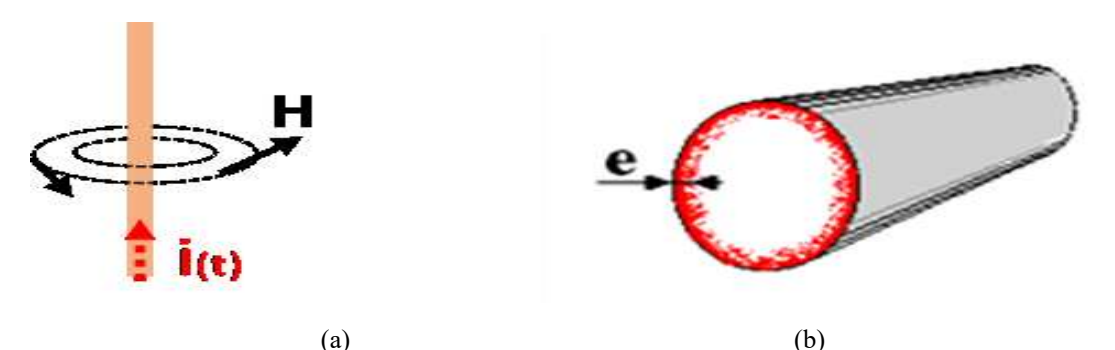


Figure 3: Skin Effect: (a) Effect of the current i(t) in a conductor; (b) Skin depth (δ) [2]. The skin depth is calculated as follows:

$$\delta = \sqrt{\frac{\rho}{\mu_0 \cdot \mu_r \cdot \pi \cdot f}} \simeq \frac{66}{\sqrt{f}} [\mu m] \qquad (4)$$

where μ_r is the relative permeability of copper (μ_r = 1) and f is expressed in MHz.

 $\delta \simeq 29 \ \mu \text{m} @ 5 \ \text{MHz}$, a value more than 12 times smaller than the diameter of the copper used for the fabrication of our component. The effective cross-section of the copper is thus reduced from 0.44 mm² to 0.07 mm² (i.e., S_O/6), a reduction that increases the resistance at 5 MHz by a factor of approximately 6.

Two models in the literature [3], [4] that incorporate the skin effect are particularly noteworthy:

Snelling Model:

$$\begin{split} R_{(f)} &= R_{DC} \left[1 + \frac{d}{\delta} \right] \\ R_{(f)} &= R_{DC} \left[1 + \frac{(r_0/\delta)^4}{48 + 0.8(r_0/\delta)^4} \right] \end{split}$$
Hurley Model:

where d represents the diameter of the copper and ro represents the radius of the copper.

Although slightly different, these formulas share the common feature of accounting for the skin depth. Their implementation yields the following result:

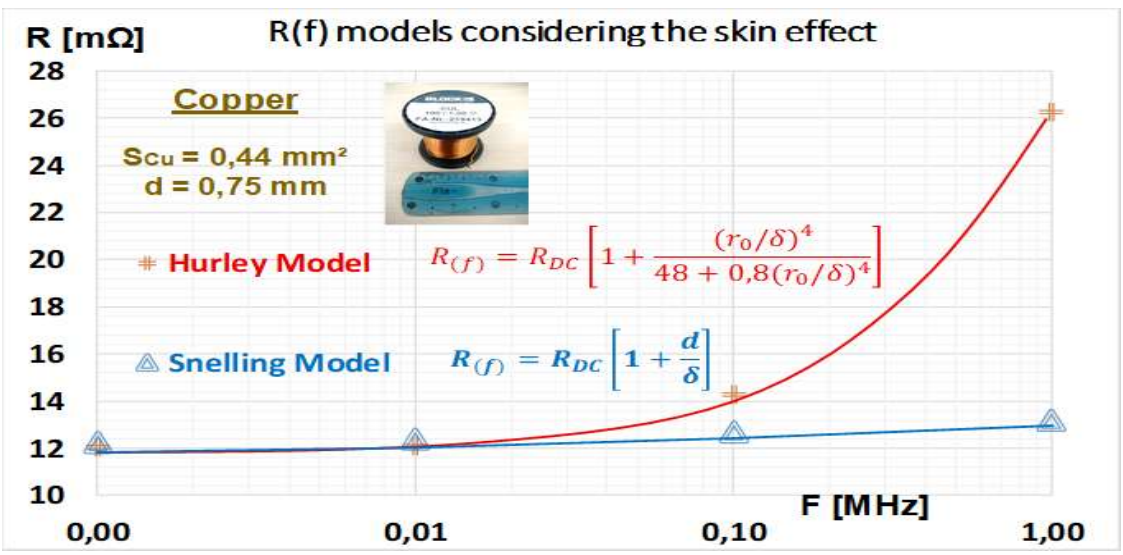


Figure 4: Models of R(f) considering the Skin Effect.

This result shows that Hurley's model predicts a faster increase in resistance starting from 10 kHz, whereas Snelling's model keeps the resistance almost constant up to 1 MHz.

Consideration of the proximity effect and parasitic capacitances:-

The proximity effect (Figure 5a) occurs when neighboring conductors carry alternating currents. For instance, when two conductors are placed side by side and one carries an AC current, it generates a varying magnetic field that can induce a current in the second conductor, and vice versa. These induced currents circulate in both conductors, which may lead to additional copper losses. Moreover, parasitic capacitances arise from capacitive coupling between adjacent turns and between the turns and the magnetic core. These effects become significant at high frequencies. Charles R. Sullivan et al. [5] illustrated these parasitic capacitances as shown in Figure 5b.

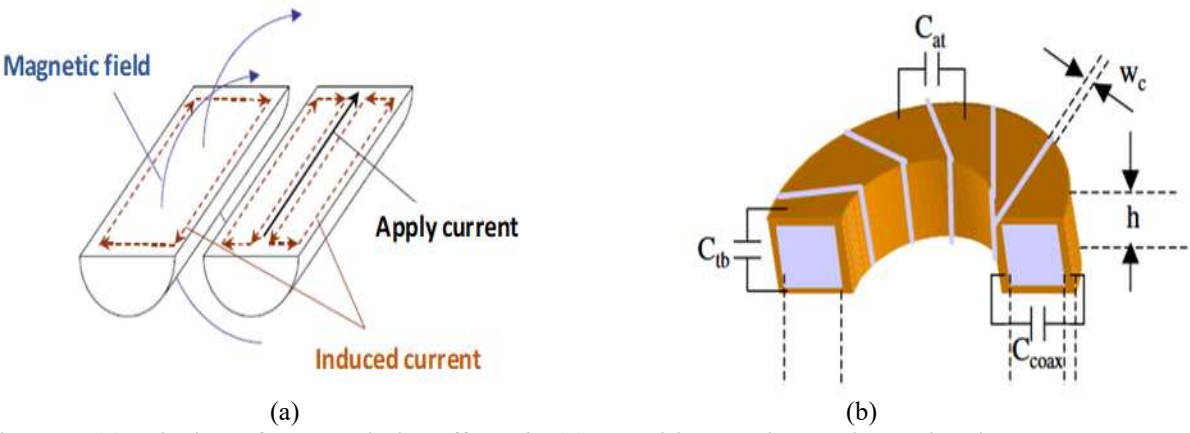


Figure 5: (a) Principle of the Proximity Effect [6]; (b) Parasitic capacitances in toroidal inductors [5].

In the literature, the model by Kuhn et al. [7] is explicit in this regard, incorporating the spacing s between turns, the conductor thickness e, and the conductor width w to empirically account for these parameters, as follows:

$$R_{(f)} = R_{DC} \left[1 + 0.1 \left(\frac{2\pi f}{\omega_{crit}} \right)^{2} \right] = R_{DC} \left[1 + 0.1 \left(\frac{2\pi f}{\frac{3.1(w+S) \rho_{cu}}{\mu_{DW}^{2} \cdot \rho_{cu}}} \right)^{2} \right] (7)$$

For a circular conductor of diameter d, the equivalent thickness w is expressed as:

$$w = (d\sqrt{\pi})/2 \tag{8}$$

Recently, Zhao et al. [8] proposed a more advanced formulation for inductors with m layers of conductors wound on top of each other around a toroidal magnetic core. For a winding layer of N turns with diameter d around a ferrite core of inner radius r, subjected to a magnetic excitation H produced by a current I, the formulation can be summarized as:

$$\begin{split} \frac{R_{AC\;(f)}}{R_{DC}} &= \frac{\gamma}{2} \left[\phi_{1(\gamma)} + \left(\frac{4\pi r H}{NI} \right)^2 \phi_{2(\gamma)} \right] - \frac{\xi}{\sqrt{2}} \left[\left(\frac{2\sqrt{\pi} H d}{I} \right)^2 \psi_{3(\xi)} \right] \\ \text{With} \quad \gamma &= \frac{w}{\delta} \quad \text{and} \quad \xi &= \frac{d\sqrt{2\pi f \mu_0 \sigma}}{2} \end{split} \tag{9}$$

The first term of Equation (9) is derived from the modified Dowell method as follows:

$$\varphi_{1(\gamma)} = \frac{\sinh{(\gamma)} + \sin{(\gamma)}}{\cosh{(\gamma)} - \cos{(\gamma)}}$$
(11)
$$\varphi_{2(\gamma)} = \frac{\sinh{(\gamma)} - \sin{(\gamma)}}{\cosh{(\gamma)} + \cos{(\gamma)}}$$
(12)

The second term of the equation corresponds to the modified Ferreira model:

$$\psi_{3(\xi)} = \frac{\text{ber}_{1}(\text{bei}_{2} + \text{ber}_{2}) + \text{bei}_{1}(\text{bei}_{2} - \text{ber}_{2})}{\text{bei}_{1}^{2} + \text{ber}_{1}^{2}}$$
(13)

It should be noted that:

$$ber_{v} = ber_{v}(\xi) \tag{14}$$

$$bei_{v} = bei_{v}(\xi) \tag{15}$$

ber, and bei, are, respectively, the Kelvin functions of order v.

For implementation purposes, the Kelvin functions can be approximated using a Taylor series expansion.

The application of Equations (7), (8), and (9) yields the following results:

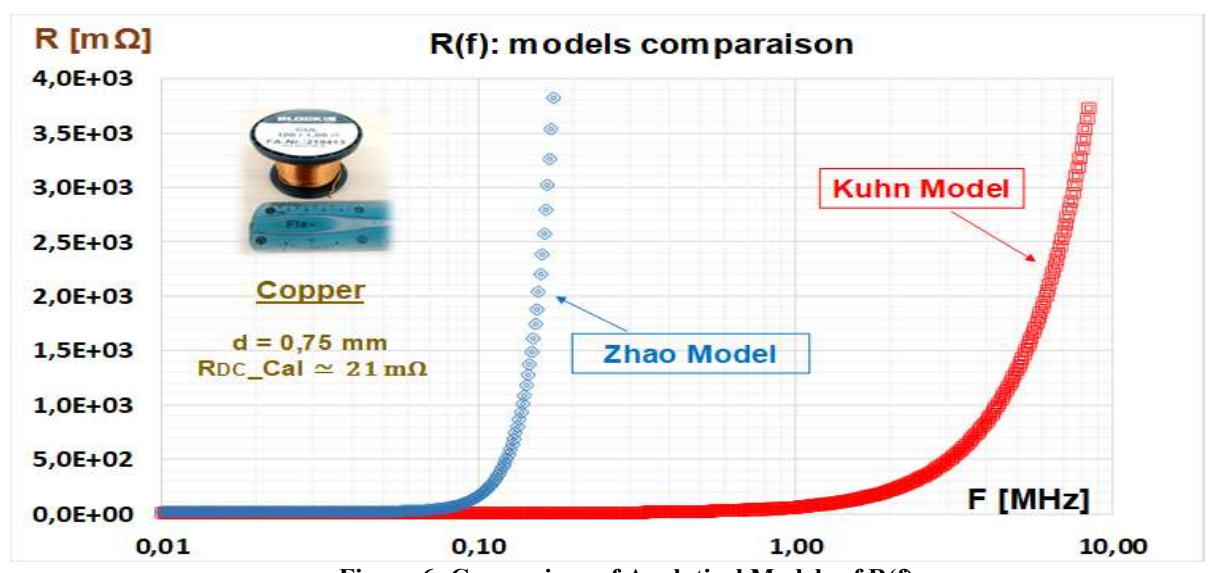


Figure 6: Comparison of Analytical Models of R(f).

These models account for the influence of frequency on the component's series resistance. However, Zhao's model rises faster than Kuhn's model. Consequently, experimental validation is required to fully confirm their accuracy.

Simulation:

The component was simulated using HFSS (High-Frequency Structure Simulator), a 3D electromagnetic software from Ansys, designed for high-frequency field analysis. It relies on the Finite Element Method (FEM) to solve Maxwell's equations in complex geometries.

Simulated Component and Extraction Model:

A 3D model of the component was created in HFSS, as shown in Figure 7. The figure illustrates the simulated component, the associated magnetic field distribution, and its behavior under low-amplitude excitation.

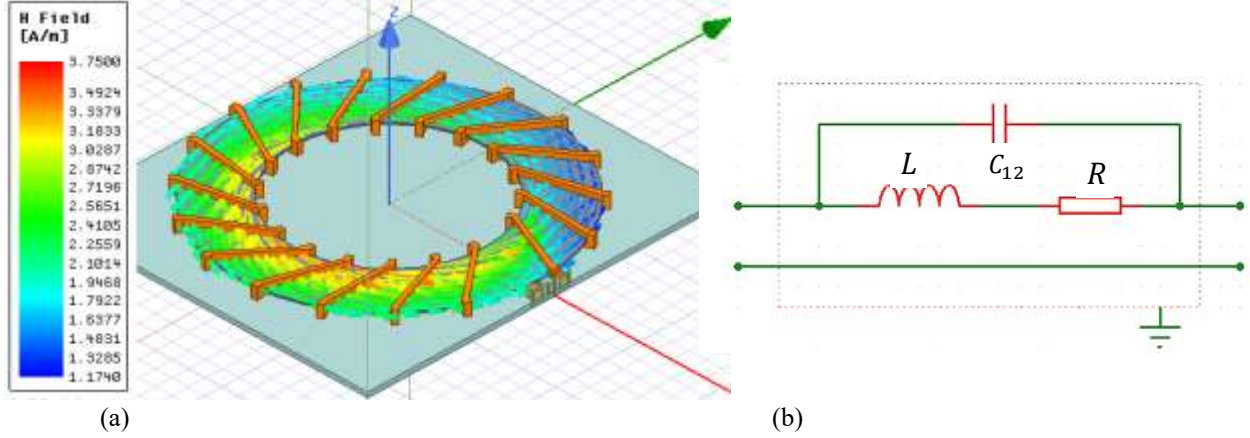


Figure 7: (a) Simulated Component; (b) Extraction Model.

The simulations were performed in the frequency domain, with extraction of the R and L parameters according to the RLC model shown in Figure 7b. For the determination of the model parameters, the admittance parameters Yij are used. Let:

$$R = \frac{-\text{Re}(\underline{y}_{12})}{\left[\text{Re}(\underline{y}_{12})\right]^{2} + \left[\text{Im}(\underline{y}_{12} + C_{12}\omega)\right]^{2}}$$

$$L = \frac{\text{Im}(\underline{y}_{12}) + C_{12}\omega}{\omega \left[\text{Re}(\underline{y}_{12})\right]^{2} + \left[\text{Im}(\underline{y}_{12} + C_{12}\omega)\right]^{2}}$$

$$\text{With} \qquad C_{12} = \frac{1}{(2f_{0}\pi)^{2}L_{0}}$$

$$(16)$$

The inductance L_0 is extracted in the low-frequency domain, where the component behaves mainly as an inductor. The resonance frequency f_0 is determined from the frequency analysis of the imaginary part of the admittance Y_{12} . It corresponds to the frequency at which $Im(Y_{12}) = 0$.

Simulation Parameters:

The key parameters summarized in the following table are used for the simulation:

Table 2: Simulation Parameters Value Catégory Parameter Name Description 99 Number of Passes Maximum number of mesh refinement passes Setup 5e-5 Convergence criterion for S-parameters Frequency 20 Hz-300 Simulation frequency range Sweep MHz Number of Points 1000 Samples per frequency sweep

Materials and experimental setup:

Test Component:

The tested component (Figure 8(g)) consists of a NiZn ferrite toroid (4C65) wound with an enameled copper wire with a 0.75 mm diameter. The toroid is first manually ground to reduce its thickness from 15 mm to approximately 1 mm, then bonded to a glass substrate (60 mm × 45 mm) using Canada balsam under gentle heating. After 24 hours

of drying, an automatic grinding process further reduces the ferrite thickness to about 200 μ m. The sample is then heated to 120 °C to detach the ferrite. Due to its fragility, a protective PLA casing (Figure 8(f)) is 3D-printed to improve mechanical stability during handling.

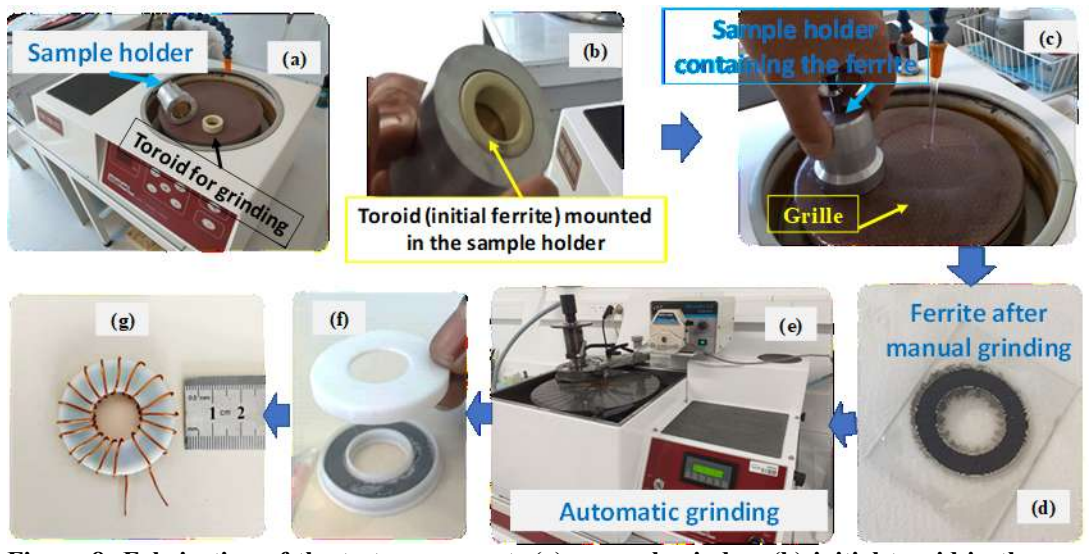


Figure 8: Fabrication of the test component: (a) manual grinder; (b) initial toroid in the sample holder; (c) manual grinding; (d) toroid prepared for automatic grinding; (e) automatic grinder; (f) toroid in 3D-printed casing; (g) test component (4C65 + 18 turns).

Measurement Setup:

The experimental setup (Figure 9) uses a 6500B impedance analyzer connected to the component via a Model 1011 test fixture, enabling measurements from 20 Hz to 120 MHz. Measurements were performed at ambient temperature (25 °C), with supply voltage stability monitored. Calibration ensures accurate determination of the electrical parameters (L and R), while a computer handles data acquisition, processing, and comparison with analytical and simulated results, providing reliable and reproducible characterization.

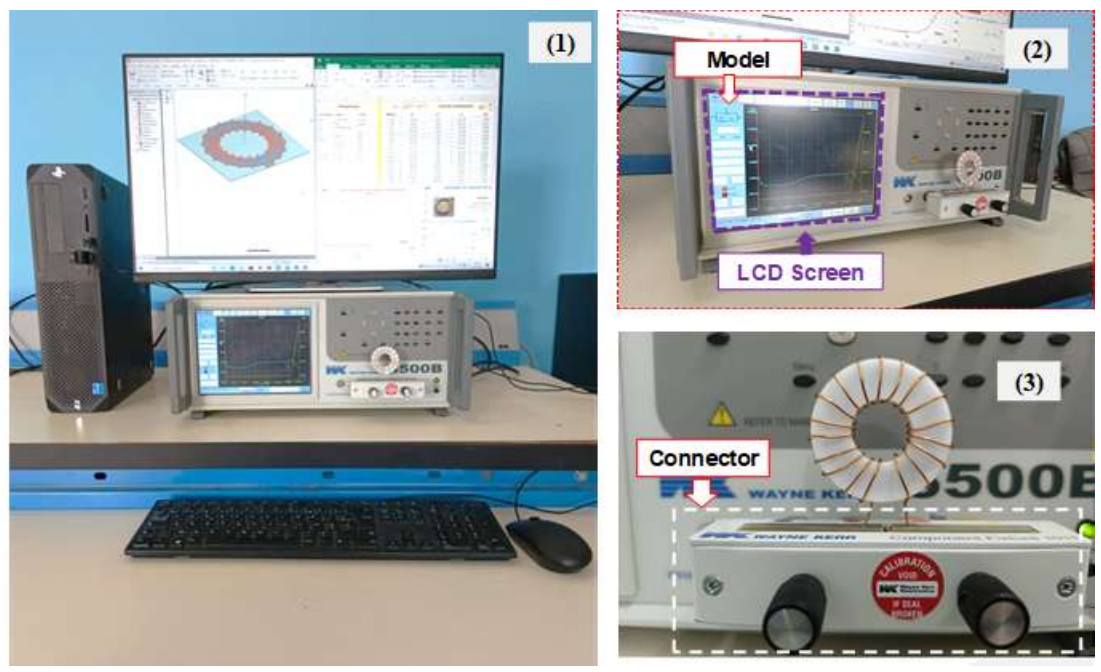


Figure 9: (1) Measurement setup: (2) impedance analyzer (6500B), (3) device under test (DUT).

Results and Analysis:-

Inductance L(f):

The obtained curves (Figure 10) are consistent in the frequency range between 100 kHz and 10 MHz. The analytical, simulated, and measured results exhibit satisfactory agreement within this frequency band.

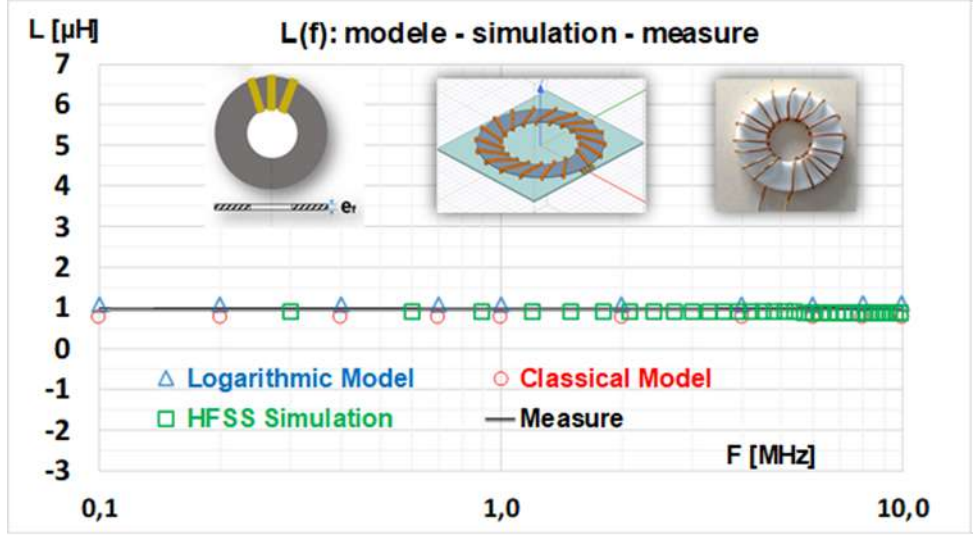


Figure 10: Comparison of inductance results as a function of frequency.

The measurements show that, over this frequency range, the inductance value is approximately the average of the two models. At 5 MHz, a deviation of about 9.2% is observed between the measured and simulated values. This relatively small discrepancy highlights the good agreement between the experimental and simulated results, thereby validating the reliability of our approach.

Series Resistance R(f):

The measured and simulated results of the component's series resistance as a function of frequency, compared with analytical models, are shown in Figure 11.

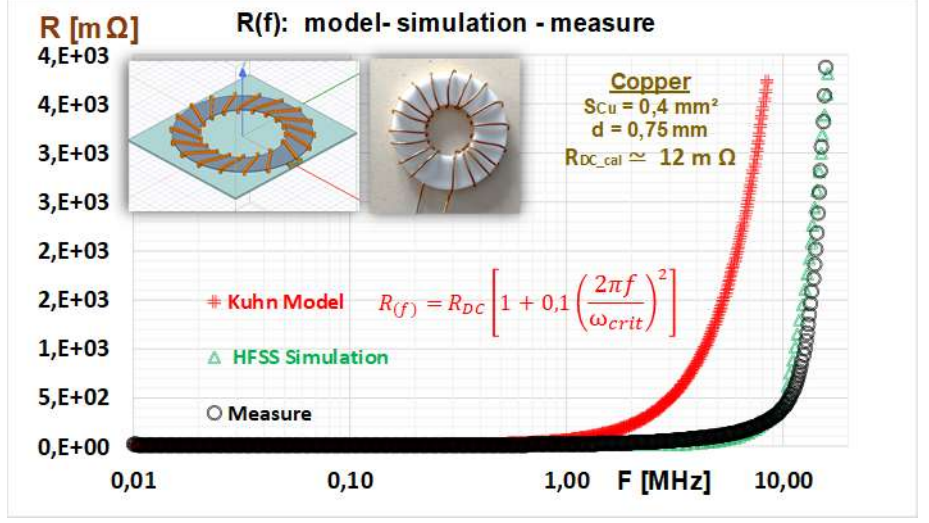


Figure 11: Comparison of series resistance results as a function of frequency.

The results show good agreement between the measured and simulated values. At low frequency, the simulated resistance (13 m Ω) and the analytically calculated value (12 m Ω) are close, while the measured resistance (21 m Ω) is higher, with a deviation of about 61.5% attributed to the component encapsulation, which increases the effective conductor length. However, Kuhn's analytical model fails to accurately predict the series resistance R(f), highlighting the limitations of analytical approaches at high frequencies.

Discussion:-

The results highlight the complementarity of the approaches used to characterize the frequency behavior of the thin toroidal inductor. Up to 10 MHz, the three methods—analytical modeling, HFSS simulation, and experimental measurements—show good agreement in the evolution of the inductance L(f), validating the reliability of our hybrid approach within this frequency range. Beyond this threshold, significant deviations arise, mainly due to the nonlinearity of the magnetic material and the increasing influence of capacitive effects. For the series resistance R(f), comparative analysis reveals important limitations of existing analytical models. Models by Zhao and Kuhn, although theoretically accounting for skin and proximity effects, fail to accurately reproduce the measured behavior of our structure, especially above 1 MHz. This divergence can be attributed to factors specific to thin geometries: non-uniform magnetic field distribution in the thin core, enhanced capacitive coupling between turns, and particular sensitivity to edge effects. The study thus demonstrates that conventional models, developed for standard thicknesses, require adaptation for accurate application to small-scale components.

Conclusion:-

This work provided a comprehensive characterization of a thin toroidal inductor using a hybrid approach combining analytical modeling, 3D simulation, and experimental validation. Good agreement was observed for the inductance L(f) up to 10 MHz, confirming the method's reliability. For the series resistance R(f), existing analytical models proved insufficient, highlighting the need for approaches that explicitly consider inter-turn capacitances. The proposed methodology offers a solid foundation for predictive modeling and the optimization of thin high-frequency inductors.

References:-

- [1]X. Yu, J. Kim, F. Herrault, et M. G. Allen, « Silicon-embedded toroidal inductors with magnetic cores: Design methodology and experimental validation », in 2014 IEEE Applied Power Electronics Conference and Exposition APEC 2014, Fort Worth, TX, USA: IEEE, mars 2014, p. 763-767. doi: 10.1109/APEC.2014.6803394.
- [2]D. D. Yaya, « Conception, réalisation et caractérisation d'inductances planaires à couches magnétiques », Université Jean Monnet Saint-Etienne, France, 2013.
- [3]W. G. Hurley et W. H. Wölfle, Transformers and inductors for power electronics: theory, design and applications. John Wiley & Sons, 2013. Consulté le: 27 octobre 2025. [En ligne]. Disponible sur: 10.1002/9781118544648 [4]E. C. (Eric C. Snelling, Soft ferrites: properties and applications. Iliffe, 1969. Consulté le: 27 octobre 2025. [En ligne]. Disponible sur: https://cir.nii.ac.jp/crid/1971430859790257689
- [5]C. R. Sullivan, W. Li, S. Prabhakaran, et S. Lu, « Design and Fabrication of Low-Loss Toroidal Air-Core Inductors », in 2007 IEEE Power Electronics Specialists Conference, Orlando, FL, USA: IEEE, 2007, p. 1754-1759. doi: 10.1109/PESC.2007.4342265.
- [6]A. A. Abderahim, « Etude des pertes dans les enroulements des composants passifs planaires », Université de Lyon, France, 2016.
- [7]W. B. Kuhn et N. M. Ibrahim, « Analysis of current crowding effects in multiturn spiral inductors », IEEE Trans. Microw. Theory Tech., vol. 49, n° 1, p. 31-38, janv. 2001, doi: 10.1109/22.899959.
- [8]Y. Zhao, Z. Ming, et B. Han, « Analytical modelling of high-frequency losses in toroidal inductors », IET Power Electron., vol. 16, n° 9, p. 1538-1547, juill. 2023, doi: 10.1049/pel2.12493.